Remote Sensing of Environment 315 (2024) 114457

Contents lists available at ScienceDirect

Remote Sensing of Environment

journal homepage: www.elsevier.com/locate/rse

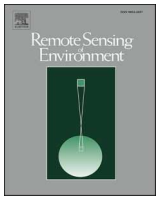

Observation-based quantification of aerosol transport using optical flow: A satellite perspective to characterize interregional transport of atmospheric pollution

Tianhao Zhang [a,*], Yu Gu [a], Bin Zhao [b,c,*], Lunche Wang [d], Zhongmin Zhu [e,f], Yun Lin [a], Xing Chang [g], Xinghui Xia [h], Zhe Jiang [i], Hongrong Shi [i], Wei Gong [e,j]

[a] Joint Institute for Regional Earth System Science and Engineering, University of California Los Angeles, Los Angeles, CA 90095, USA
[b] State Key Joint Laboratory of Environmental Simulation and Pollution Control, School of Environment, Tsinghua University, Beijing 100084, China
[c] State Environmental Protection Key Laboratory of Sources and Control of Air Pollution Complex, Beijing 100084, China
[d] Hubei Key Laboratory of Regional Ecology and Environmental Change, School of Geography and Information Engineering, China University of Geosciences, Wuhan 430074, China
[e] State Key Laboratory of Information Engineering in Surveying, Mapping and Remote Sensing, Wuhan University, Wuhan 430079, China
[f] College of Information Science and Engineering, Wuchang Shouyi University, Wuhan 430064, China
[g] Laboratory of Transport Pollution Control and Monitoring Technology, Transport Planning and Research Institut, Ministry of Transporte, Beijing 100028, China
[h] School of Artificial Intelligence, Hubei University, Wuhan 430062, China
[i] Institute of Atmospheric Physics, Chinese Academy of Sciences, Beijing 100029, China
[j] School of Electronic Information, Wuhan University, Wuhan 430079, China

ARTICLE INFO

Edited by Menghua Wang

Keywords:
Atmospheric pollution
Interregional transport
Aerosol dynamic optical flow
Aerosol transport index (ATI)
Satellite synergistic observations

ABSTRACT

Interregional transport plays a significant role in haze formation with varying and disputable contribution extent. Current research on quantitatively analyzing interregional atmospheric pollution transport has mainly relied on meteorological and chemical models. However, these models are typically affected by uncertainties due to the assumptions and simplifications inherent in the numerical simulations and source emission estimations. In this study, a comprehensive optical flow framework is developed to offer a new perspective on quantitative characterization of interregional transport of atmospheric pollution based on synergistic observations from geostationary and sun-synchronous satellites. In this framework, the high-frequency continuous aerosol observing images are regarded as video in computer vision, and an aerosol dynamic optical flow algorithm is proposed by incorporating aerosol-specific assumptions and constraints, overcoming the limitation that traditional optical flow methods are typically confined to rigid bodies. Results demonstrate that the developed optical flow framework could distinguish the aerosol transport process from other dynamic processes of aerosol development and accurately capture the fast-changing details of transport processes. Moreover, the satellite-based optical flow framework achieves aerosol transport results comparable to those of widely accepted model-based methods, demonstrating the physical interpretation of pixel-based optical flow results and highlighting its effectiveness in quantitative characterization of the atmospheric pollution transport process via the Aerosol Transport Index (ATI). Furthermore, a case analysis of long-term assessments of interregional transport of atmospheric pollution indicates that Beijing acts as a "sink" of atmospheric pollution, and a downward trend could be found from the annually averaged transported aerosol net loadings due to the emission reduction policy. Compared with model-based methods, the satellite-based optical flow framework is directly grounded in observations and does not rely on emission inventories that take years to update. Therefore, it not only helps improve understanding the patterns of atmospheric pollution interregional transport, but also provides a more efficient and economical way to assess the effectiveness of regional joint control policy.

* Corresponding authors.
E-mail addresses: zhangth@ucla.edu (T. Zhang), bzhao@mail.tsinghua.edu.cn (B. Zhao).

https://doi.org/10.1016/j.rse.2024.114457
Received 15 July 2024; Received in revised form 26 August 2024; Accepted 30 September 2024
Available online 3 October 2024

1. Introduction

Atmospheric pollution, which is primarily contributed by anthropogenic aerosols generated from human activities, can cause complicated impacts on radiation budget and climate change (Albrecht, 1989; Knippertz et al., 2015; Masson-Delmotte et al., 2021; Ramanathan et al., 2001). Additionally, atmospheric pollution, especially the fine particular matter, has a variety of adverse implications on human health, as one of the leading risk factors for global burden of disease, thereby influencing morbidity and mortality (Cohen et al., 2017; Kan et al., 2012; Pope et al., 2002; Zhang et al., 2018). It is increasingly recognized that atmospheric pollution in a specific region include not only those from local sources but also a substantial proportion of exogenous aerosols from surrounding and distant sources delivered via transport processes (Huang et al., 2020; Yu et al., 2012; Zhang et al., 2017). And the regional-scale transport process is usually complex that contributes to the local atmospheric pollution with varying extent under different meteorological and emission conditions, thus leading to uncertainties in the clarification of reasons for severe haze (Chang et al., 2019; Li et al., 2015). Therefore, quantifying and characterizing the interregional transport of atmospheric pollution are necessary and undoubtedly meaningful for the regional atmospheric pollution joint control and policy making.

In recent decades, various studies have been conducted to describe and characterize the regional atmospheric pollution transport, where the most widely used type of methods have mainly relied on meteorological and chemical models, such as the backward trajectory models (Draxler and Hess, 1998; Stein et al., 2015), sensitivity analysis within chemical transport models (Yang et al., 1997; Zhao et al., 2015), source-oriented models (Zhang et al., 2014), direct calculation of transport flux through using chemical transport models (Berge and Jakobsen, 1998; Jenner and Abiodun, 2013; Wang et al., 2009), etc. Nonetheless, these model-based methods are typically affected by uncertainties due to the assumptions and simplifications inherent in the numerical simulations and source emission estimations, such that the atmospheric models do not always reliably capture the pattern and/or quantity of aerosols owing to highly complicated atmospheric physicochemical processes, thereby resulting in large variation in simulation results among different models.

Satellite-based remote sensing is efficient in providing spatially continuous aerosol observations at large scale. With the launch of new-generation geostationary satellites, such as the Himawari-8/9 and Geostationary Operational Environmental Satellite (GOES) series, the frequency of aerosol observations has increased remarkably to every 5–10 min. Because the period over which aerosol fields change notably is usually approximately 30 min (Kikuchi et al., 2018; Prather, 2009), the temporally continuous aerosol images derived from geostationary satellites could be treated as video (Zhang et al., 2019). Accordingly, the computer-vision-based optical flow method, which is generally applied for motion detection and motion compensation based on the movement of brightness pattern of pixels from continuous image sequencies (Horn and Schunck, 1981), possesses huge potential for addressing the problem of how to estimate dynamic aerosol transport from static satellite aerosol observations (Zhang et al., 2020). Nevertheless, a series of challenges and difficulties must be overcome when incorporating the computer-vision-based optical flow method into the field of atmospheric aerosol research. The most critical problem is that optical flow methods were originally designed for a rigid body assuming that the form of the target object never changes during the motion process, whereas aerosols can develop and change over time via physicochemical processes or anthropogenic emissions. Moreover, the optical flow is typically calculated on intact images for utilizing spatiotemporally adjacent information, which is significantly hindered by the substantial amount of data blank in satellite-derived aerosol products caused by cloud cover or high reflected land surface (Gupta et al., 2019).

In this study, a comprehensive optical flow framework, where a novel aerosol dynamic optical flow algorithm is proposed to quantify aerosol transport using multi-satellite synergistic observations, is developed to provide a satellite perspective to quantitatively characterize interregional transport of atmospheric pollution. Specifically, the high-frequency aerosol observations with improved spatial coverage and accuracy are firstly generated by merging data from geostationary and sun-synchronous satellites and fusing the retrievals of active and passive sensors. The aerosol dynamic optical flow algorithm is then proposed by incorporating the aerosol variation over time and topographical information into the classic optical flow model. Additionally, an aerosol transport index (ATI), combined with a transported loading calculation scheme, is proposed and utilized to establish the physical interpretation of the optical flow results, and corresponding results from coupled meteorological–chemical model simulations are employed for comparison and discussion. Furthermore, the boundary transport contribution and net transported aerosol loadings for Beijing is analyzed and discussed to demonstrate the effectiveness and efficiency of optical flow framework in characterizing the interregional transport patterns of atmospheric pollution.

2. Datasets and study area

2.1. Satellite-derived datasets

Himawari-8 is a new-generation geostationary (GEO) meteorological satellite that carries the Advanced Himawari Imager (AHI) sensor, which was launched by the Japan Aerospace Exploration Agency. This instrument was specifically designed to provide complete coverage of the Asian-Pacific area, with a resolution of 10 min and centered on the equator at around 140.7° E. (Bessho et al., 2016; Yoshida et al., 2021). In this study, the adopted Himawari-8 AHI AOD datasets at 550 nm, possessing a spatial resolution of 5-km and a temporal resolution of 10 min, was retrieved by the GeoMRA algorithm proposed in our previous research, which demonstrates better accuracy and higher spatial coverage, combined with smoother spatiotemporal variations (Zhang et al., 2022), comparing to the officially released AOD products. To minimize error propagation caused by erroneous AOD pixels from original AOD data, a stricter cloud screening process is applied. Specifically, the 10-min cloud mask derived from the Himawari-8 cloud products is utilized to further screen the corresponding 10-min AOD dataset to eliminate possible impacts from cloud contamination on aerosol observations (Ishida and Nakajima, 2009). The cloud screened AHI AOD dataset is generated by excluding the original AHI AOD value on those pixels where the corresponding cloud mask data are marked as cloud flag.

The Moderate Resolution Imaging Spectroradiometer (MODIS) operating on the Terra and Aqua satellites follow sun-synchronous orbits (SSO) and pass over the equator at approximate 10:30 and 13:30 local time, respectively. This allows them to provide accurate global scale observations of aerosols twice a day. The AOD dataset derived from the dark target (DT) algorithm is generally accurate in densely vegetated areas, whereas the AOD dataset derived from the deep blue (DB) algorithm has unique benefits for retrieving aerosol information over high-reflected land surfaces (Christopher and Jones, 2010; Hsu et al., 2013; Levy et al., 2007). Thus, the MODIS DT_DB_merged_AOD datasets with 10-km spatial resolution and relatively high quality assurance flags, obtained from the Terra and Aqua MODIS aerosol products (i.e., MOD04 and MYD04), were utilized in this study to obtain AOD datasets derived from SSO satellites with assured accuracy and higher data completeness (Huang et al., 2019; Mhawish et al., 2017), to provide supplementary aerosol observing information during the subsequent GEO AOD recovery process.

The Cloud-Aerosol Lidar with Orthogonal Polarization (CALIOP) onboard the Cloud-Aerosol Lidar and Infrared Pathfinder Satellite Observation (CALIPSO) platform is an active-scanning-mode SSO satellite sensor, which can provide aerosol profile measurements at around

01:30 a.m. and 1:30 p.m. local time. This study utilized both the daytime and nighttime aerosol data, extracted from the CALIOP aerosol profile product (APro), to assist in improving spatial completeness for GEO AOD datasets, through leveraging their unique advantages in monitoring aerosols under thin cloud, haze, and nocturnal situations (Campbell et al., 2012). Moreover, the daytime CALIOP vertical feature mask product was adopted to generate precise cloud/aerosol identification information for conducting further cloud screening on AOD products derived using passive optical sensors mentioned above, particularly in situations involving optically transparent clouds (Kacenelenbogen et al., 2011; Vaughan et al., 2009).

All the satellite-based datasets utilized in the experiment, which are summarized and listed in Table 1, follow the data integration strategy that involves initially reprojecting all the datasets into the World Geodetic System 1984 geographic coordinate system, followed by resampling to maintain consistency with the 5-km spatial resolution of the AHI geographic grids.

2.2. Study area

As illustrated in Fig. 1, the Beijing–Tianjin–Hebei (BTH) region on the North China Plain is selected as the representative experimental area in this study. The BTH region, which has undergone rapid industrialization and urbanization in recent years, periodically suffers atmospheric pollution episodes (Cai et al., 2017a). And the unique topographic characteristics of BTH, with its partial enclosure by the mountains to the west and north, blocks the dispersion of atmospheric pollutants to a certain extent, thereby leading to the aggravation of atmospheric pollution during the haze period, especially in Beijing and part of southern Hebei regions (Han et al., 2015). Thus, it is significant to characterize the interregional atmospheric pollution transport in the BTH region, and provide accurate estimations for interregional transport contribution of pollution to develop effective joint emission control strategies.

3. Research methodology

As shown in the schematic diagram as Fig. 2, the comprehensive framework is developed to provide observation-based quantification of aerosol transport. The 10-min AOD datasets with improved accuracy and spatial coverage are obtained by spatiotemporally fusing the observations from the Himawari-8, MODIS, and CALIOP satellites following the Bayesian maximum entropy (BME) theory. The aerosol dynamic optical flow algorithm is subsequently developed and applied, based on temporally successive AOD images, to quantitatively estimate the velocity field for each valid AOD pixel. The aerosol transport index (ATI), as well as the corresponding transported loading calculation scheme, is accordingly proposed to offer a consistent description between the pixel-based optical flow results and the model simulated results, where selected results from the Weather Research and Forecasting–Community Multiscale Air Quality (WRF-CMAQ) model simulation are applied for comparison and discussion of the physical interpretation of the optical flow results. Specific descriptions of the related methodologies used in this study are described in the following.

Table 1
Summary of all the satellite-derived datasets adopted in the aerosol dynamic optical flow calculation.

Instrument	Dataset	Spatial Resolution	Temporal Resolution	Description
Himawari-8 AHI	GeoMRA AOD	5 km	10 min	(Zhang et al., 2022)
	CLP_L2	5 km	10 min	Version 1.0
Terra MODIS	MOD04_L2	10 km	daily (a.m.)	Collection 6.1
Aqua MODIS	MYD04_L2	10 km	daily (p.m.)	Collection 6.1
CALIOP	CAL_LID_L2_05kmAPro	5 km	daytime/nighttime	Version 4.2
	CAL_LID_L2_VFM	5 km	daily (p.m.)	Version 4.2

3.1. Satellite-derived AOD data recovery

The computer-vision-based optical flow method was originally designed for intact natural images with complete valid pixels. Therefore, the substantial amount of data blanks in satellite-derived AOD products, primarily caused by cloud obscuration and the intrinsic limitations of aerosol retrieval algorithms, leads to failure of the optical flow algorithm in most cases. To overcome this problem, prior to the optical flow calculation, the spatiotemporal fusion blending GEO with SSO satellite observations based on BME theorem has been applied to dramatically improve the spatiotemporal coverage of Himawari-8 AHI 10-min AOD datasets with ensured accuracy and reconstructed aerosol diurnal variation trends. The related algorithms, described in our previous studies (Xia et al., 2023; Xia et al., 2021; Zhang et al., 2023), include the following two main procedures, as shown in Fig. 2.

The data preprocess aims to guarantee the spatial and temporal consistency as well as the data reliability from multi-source satellite observations, primarily including data integration, temporal matching, and further cloud screening. It is of vital significance to minimize the effects of erroneous AOD pixels resulting from misidentifying clouds as aerosols, because the abnormal values from the AOD images probably lead to error propagation during the AOD recovery process and possibly create huge uncertainty in the pixel-based optical flow calculation. Thus, the 10-min AHI AOD dataset has undergone initial screening using matching 10-min cloud mask, and subsequently examined strictly by the threshold of adjacent spatiotemporally error variance (Kikuchi et al., 2018). In addition to that, the cloud mask derived from passive satellite sensors may misidentify thin clouds as aerosols, leading to erroneous values in the AOD products. In contrast, active satellite sensors offer unique advantages in discriminating between aerosols and clouds. To enhance the reliability of our AOD data, we adopt the cloud mask derived from CALIOP to conduct further cloud screening on Aqua MODIS AOD data and temporally adjacent AHI AOD data within thirty minutes before and after the CALIOP passing time. This additional screening aims to minimize error propagation during the subsequent AOD fusion and optical flow calculations. In terms of spatial data integration, both CALIOP-derived data and MODIS data are first reprojected into the same geographic coordinate system and then resampled to match the AHI 5 km geographic grids. The CALIOP data is morphologically dilated to 0.5° on both side of observing nadir track for better spatial coverage, which is described in details in our previous study (Xia et al., 2021). Although the CALIOP-based cloud screening can only be applied to a portion of AHI AOD data due to the relatively limited spatial coverage and observing frequency of CALIOP data, yet this step could reduce the number of erroneous AOD values in the original AHI AOD data to a certain extent, contributing essentially to more reliability in the subsequent data fusion process and optical flow calculation by avoiding potential error propagation.

The GEO-SSO BME AOD recovery is a data fusion algorithm that merge the aerosol observations from different satellites based on the BME theorem (Christakos, 2002; Christakos and Li, 1998; Spadavecchia and Williams, 2009). This algorithm utilizes AOD data from multiple sources, including SSO passive sensor MODIS, SSO active sensor CALIOP, and GEO passive sensor AHI, to sufficiently excavate complementary information. To be specific, the AOD expectation for a missing pixel is estimated by constructing the posterior probability density function through valid spatiotemporally adjacent AOD pixels and modeling the joint probability density function via a statistical spatiotemporal covariance model for autocorrelation of AOD soft data. The AOD probabilistic soft data for AHI, CALIOP, and MODIS is constructed by the

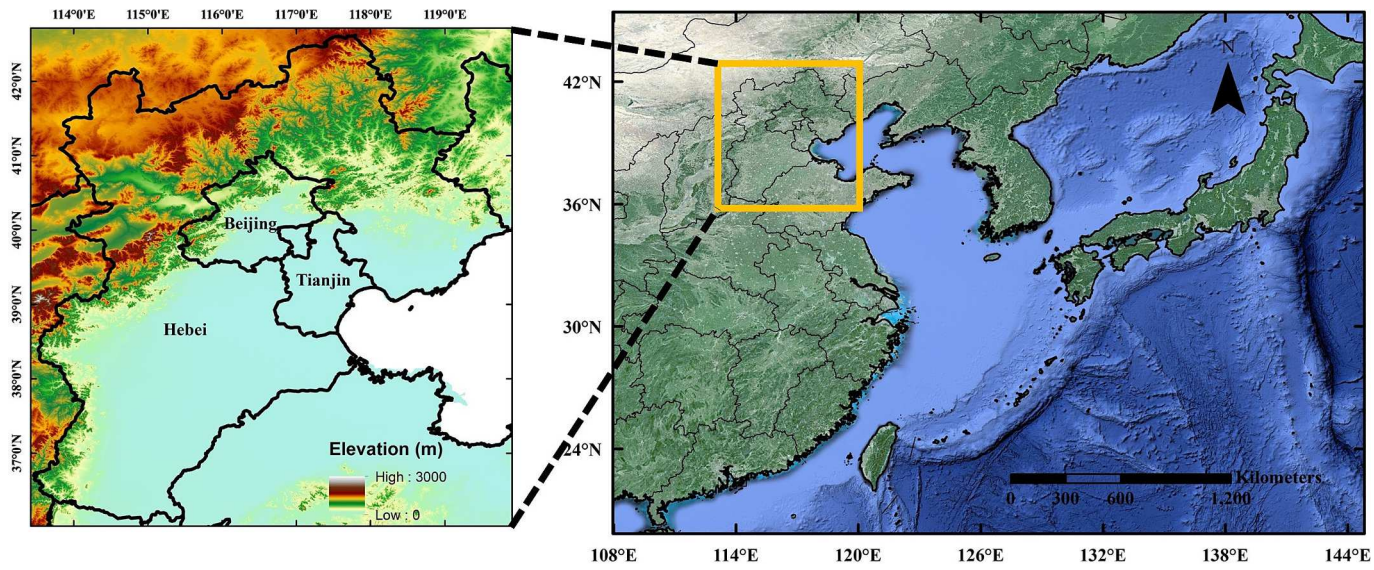

Fig. 1. The topographic elevation of the experimental area, combined with its location in East Asia.

weight via corresponding inversed spatiotemporal distance, where the data accuracy discrepancy arising from different satellite AOD datasets is incorporated (Tang et al., 2016). The basic principles for AOD fusion via BME theorem are provided in Supplementary Material Text S1, while elaborate procedures and specific parameters can be referred in our previous studies (Xia et al., 2023; Zhang et al., 2023). The GEO-SSO BME AOD recovery procedure can provide a 10-min dataset with better spatial completeness and ensured accuracy, combined with the reconstruction of aerosol diurnal variation trends to a certain extent. It needs to be mentioned that the subsequent optical flow method is applied to valid AOD pixel only if its surrounding zones in both temporally adjacent AOD images are filled by complete valid AOD values in this study, since the optical flow algorithm is typically applicable for intact images. In other words, the higher spatiotemporal coverage the more areas are applicable for the subsequent optical flow algorithm, on the premise that the recovered AOD data possesses comparable data accuracy as the original AOD data before fusion. Moreover, as some data gaps remain in the 10-min AOD dataset even after the recovery process, which prioritizes data reliability, a smaller size of calculation zone could enable more AOD pixels to fulfill the prerequisites for optical flow calculation.

3.2. Aerosol dynamic optical flow algorithm

The optical flow literarily indicates that the object motion projects to two-dimensional plane causing the brightness variation (Fleet and Weiss, 2006; Gibson, 1950), while the classic optical flow method is to estimate the motion velocity of object based on video images, under a basic assumption of brightness conservation that the intensity (or grayscale value) of one same pixel remains constant within two successive video frames (Barron et al., 1994; Lucas and Kanade, 1981). It can be typically expressed by:

$$I(x+dx, y+dy, t+dt) = I(x, y, t) \tag{1}$$

where the $I(x, y, t)$ represents the brightness of one pixel with coordinate (x, y) in the current frame image at time t, while the $I(x+dx, y+dy, t+dt)$ represents the brightness of this pixel with a displacement (dx, dy) in the next frame image after a relatively short time interval dt. With a first-order Taylor development on the left term of Eq. (1), the classic optical flow constraint equation could be obtained as:

$$\frac{\partial I}{\partial x}u + \frac{\partial I}{\partial y}v + \frac{\partial I}{\partial t} = 0 \tag{2}$$

where the $u \triangleq dx/dt$ and $v \triangleq dy/dt$ is the apparent motion velocity that remains to be solved, while the $\partial I/\partial x$, $\partial I/\partial y$, and $\partial I/\partial t$ represents the spatial and temporal gradient of brightness, respectively. These two unknown velocity components (u, v) cannot be uniquely solved by Eq. (2) alone, which is called the aperture problem of optical flow calculation (Beauchemin and Barron, 1995). A supplementary regularization term is thereby introduced as a smooth constraint on the velocity field, deducing the final cost function J for the variational optical flow method could be constructed as follows:

$$\min_{(u,v)} J = J_{con} + \lambda J_{reg} = \iint_{\Omega} \left[\left(\frac{\partial I}{\partial x}u + \frac{\partial I}{\partial y}v + \frac{\partial I}{\partial t} \right)^2 + \lambda \left(|\nabla u|^2 + |\nabla v|^2 \right) \right] dxdy \tag{3}$$

where J_{con} is called the data constraint term; J_{reg} is typically called the regularization term; Ω represents the whole image plane; $\nabla u, \nabla v$ indicates the spatial gradient of velocity field; and λ is a weight to balance the smooth constraint.

However, an aerosol field develops and changes temporally owing to physicochemical processes and/or anthropogenic emissions, which means that AOD values (pixel brightness) will change during transport, thereby failing to satisfy the fundamental assumption of classic optical flow methods. Considering the characteristics of aerosol development, we propose a novel aerosol dynamic optical flow algorithm that constructs an aerosol-specific core assumption, which can be expressed as follows:

$$I(x+dx, y+dy, t+dt) = A(x, y, t) \bullet I(x, y, t) + B(x, y, t) \tag{4}$$

where the AOD value $I(x, y, t)$ at time t could have a linear variation after moving to $(x+dx, y+dy)$ after a relatively short time interval dt, and the linear variation coefficients A and B are the function of space and time. If dominant physical or chemical processes occur during aerosol transport that lead to the increase in aerosol loading, such as newly emitted pollution or new particle formation processes, the AOD value $I(x+dx, y+dy, t+dt)$ after displacement will be larger than the original AOD value $I(x, y, t)$. Conversely, if processes that allow the decline of aerosol loading during aerosol transport take place, such as pollution diffusion or aerosol deposition processes, the AOD value after displacement will be smaller than the original AOD value. And the constraint equation could be similarly obtained as:

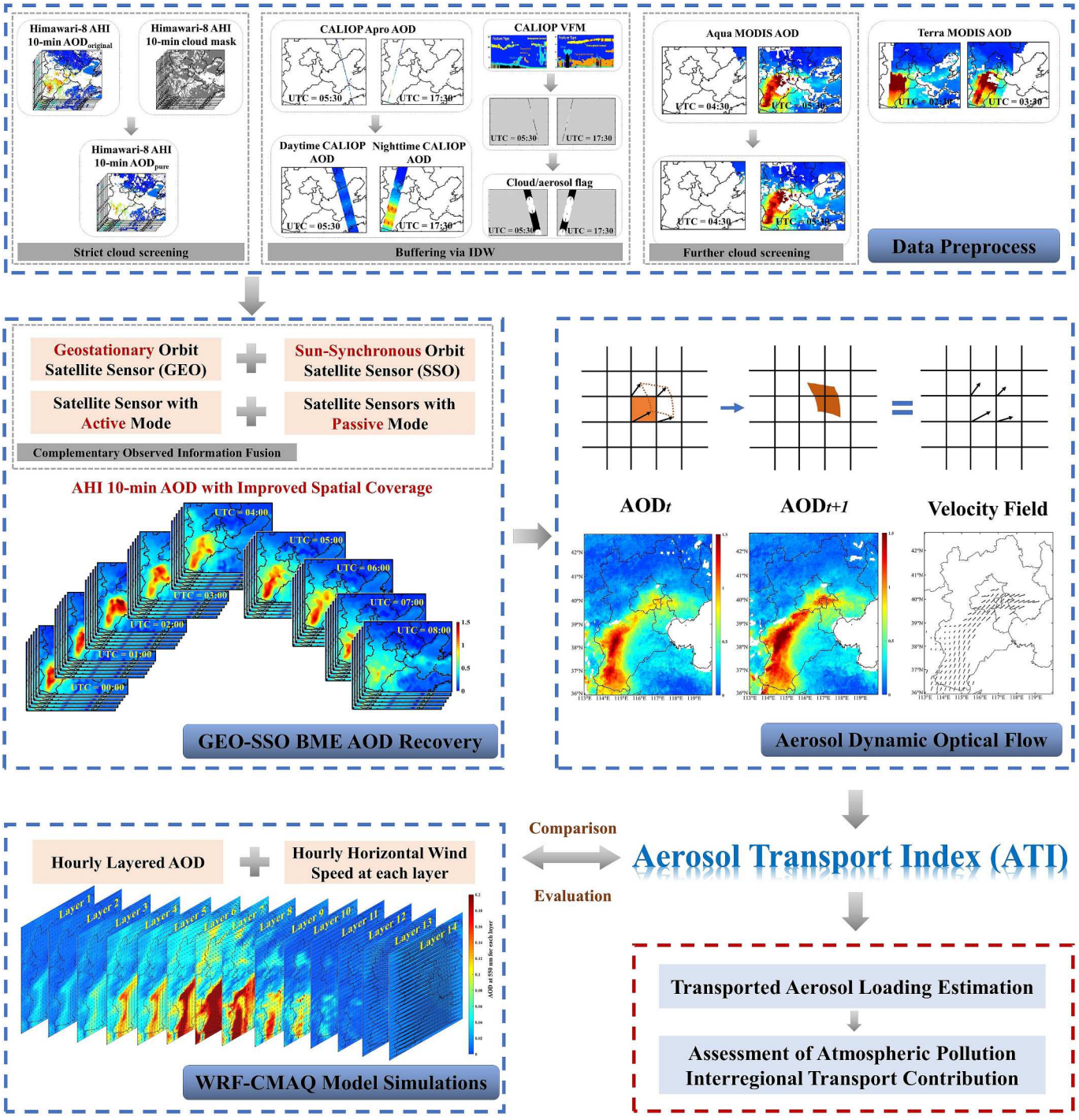

Fig. 2. Flowchart of quantifying the aerosol transport based on satellite observations, primarily including satellite-derived AOD recovery, the aerosol dynamic optical flow algorithm, comparison and evaluation against WRF-CMAQ model simulations, and the proposal of ATI combined with its application in interregional transport of atmospheric pollution.

$$\frac{\partial I}{\partial x}u+\frac{\partial I}{\partial y}v+\frac{\partial I}{\partial t}-(aI+b)=0 \tag{5}$$

where $a = lim_{dt\to 0}(A-1)/dt$ and $b = lim_{dt\to 0}B/dt$. In order to solve this optimization problem, two introduced variables are constrained by the additional regularization terms that the coefficients of variation of brightness (AOD value) remains spatially smooth. It should be noted that in situations where the topography changes drastically, the linear variation coefficients among the spatially adjacent pixels may become uncorrelated. To address this, a weight penalty is exerted on spatial gradient of variation coefficients on the pixel with relatively large terrain height gradient, by convolutionally multiplying the inverse of terrain height gradient as a weight function on the regularization term to mitigate their contradictory effects on the cost function. Assuming ∇a and ∇b indicate the spatial gradients of variation coefficients of AOD value and ω represents the global weight function based on the terrain height gradient ∇h, the cost function for aerosol dynamic optical flow could be expressed as follows:

$$\min_{(u,v,a,b)} J = J_{con}+\lambda_{reg}\bullet J_{reg}+\lambda_{var}\bullet J_{var} \tag{6}$$

$$J_{var} = J_a + J_b = \iint_{\Omega} \omega(\nabla h)^* \left(|\nabla a|^2\right) dxdy + \iint_{\Omega} \omega(\nabla h)^* \left(|\nabla b|^2\right) dxdy \tag{7}$$

The aerosol dynamic optical flow algorithm is particularly designed for aerosol transport estimation, where the brightness change of image pixels is considered during the calculation process of the velocity field, which reflects the development and variation of aerosols during the aerosol transport process. According to the Lax-Milgram lemma (Aubin, 2011), it has been proven that the optimization problem for the function styles like cost function J has a unique solution (Schnorr, 1991), satisfying the assumption in regularization terms that the variation coefficients of pixel brightness (AOD value) remain spatially smooth in Eq. (7), which is the main reason that linear function rather than other high-order functions is adopted to approximate the AOD variation during transport. Moreover, the multiscale pyramid iteration algorithm is applied to estimate the velocity field from coarse to fine, as illustrated in Fig. 3, to address the limitation that the intervals of displacement and time have to be sufficiently small to meet the approximation requirement from the first-order Taylor expansion (Brox et al., 2004; Cai et al., 2017b; Ruhnau et al., 2005). Specifically, the optical flow algorithm operates on a constructed three-layer pyramid image pairs AOD_t and AOD_{t+1}. The optical flow algorithm starts from the highest image pair in the pyramid with the lowest spatial resolution (Level 2) and computes velocity field denoted as (u_2, v_2). The Level 2 velocity field is then projected to Level 1 of the pyramid with finer resolution, denoted as $(\widehat{u_2}, \widehat{v_2})$. The velocity field (u_1, v_1) between the resampled AOD_t on Level 1 and resampled AOD_{t+1} on Level 1 is calculated by summing the initial velocity field $(\widehat{u_2}, \widehat{v_2})$ and the optical-flow-derived velocity increments $(\Delta u_1, \Delta v_1)$ as $(\widehat{u_2} + \Delta u_1, \widehat{v_2} + \Delta v_1)$. Similarly, this process is iterated to the Level 0 image pair with original spatial resolution to obtain the final velocity field (u_0, v_0). Corresponding step-by-step procedures for this algorithm is described in the Supplementary Material Text S2. Besides, it needs to be mentioned that the proposed aerosol dynamic optical flow algorithm was applied in this study only to valid AOD pixels under at least slight pollution conditions (i.e., AOD $>$ 0.4), because the optical flow method typically invalidates on spatially uniform images without textural features. This is considered acceptable because the focus of aerosol transport is on polluted air masses, which account for the absolute majority of transport contribution, rather than on the flow of clean air masses. Moreover, as the minimal typical spatial scale for AOD variation is approximately 40 km (Zhao et al., 2019), the half-length of sliding calculation window is selected as 50 km in this study to ensure discernable AOD spatial gradients within the window, thereby ensuring the effectiveness of optical flow algorithm.

3.3. WRF-CMAQ model simulation

The model-simulated hourly AOD datasets used in this study are obtained via WRF-CMAQ model simulations. Double-nesting domains are adopted in the model simulations, where the external domain covered East Asia with 27 km horizontal resolution, and the internal domain covered the BTH region at 9 km horizontal resolution. Most of the model configurations and emission inventory align with those utilized in our previous research (Ding et al., 2022; Ding et al., 2019), which are described in Supplementary Material Text S3. Moreover, the model-derived AOD segment in each vertical layer is the vertical integration of the aerosol extinction coefficient in that layer, which is calculated using the model-simulated mass concentration of each aerosol species and the corresponding mass extinction coefficient under

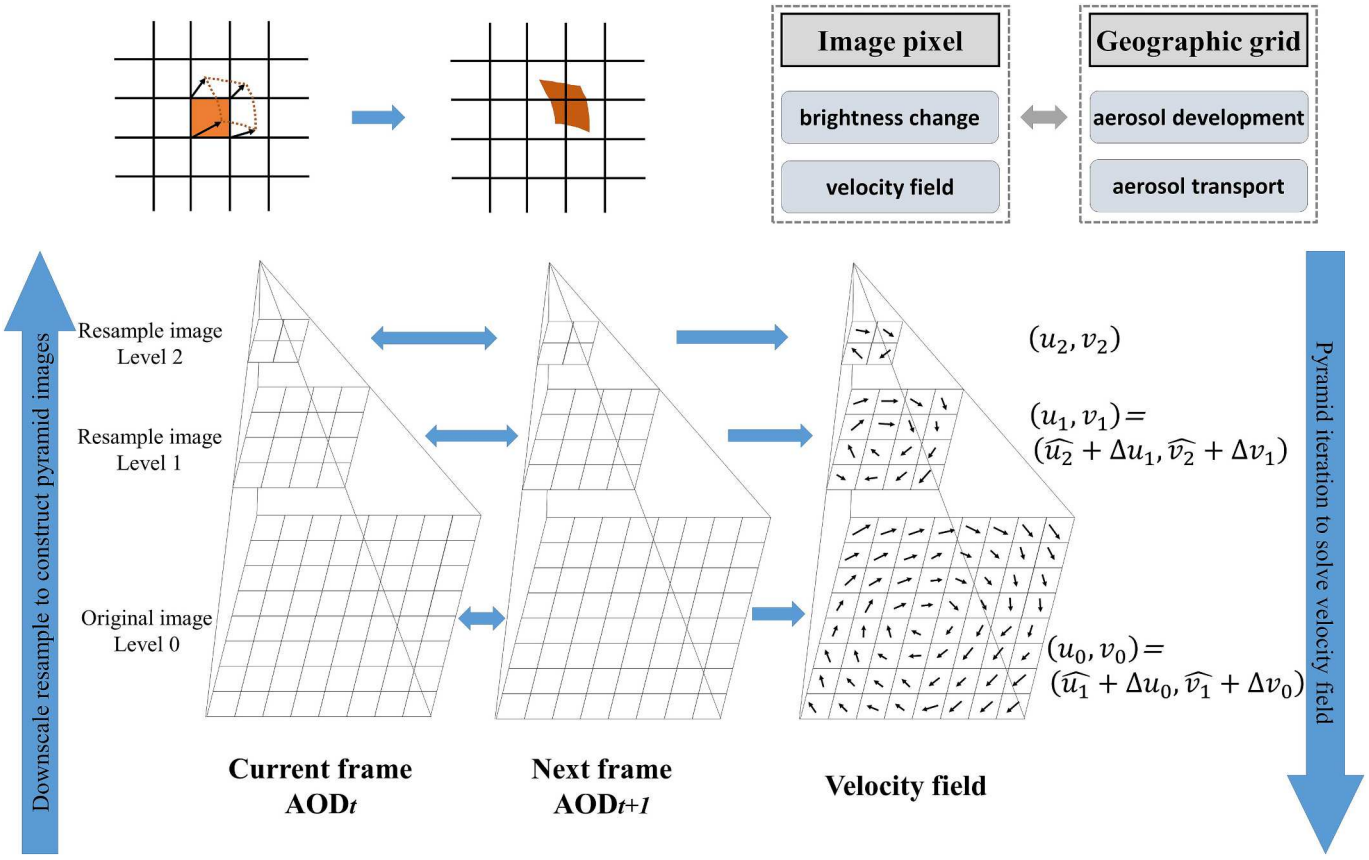

Fig. 3. Schematics of aerosol dynamic optical flow method combined with multiscale pyramid iteration procedures. The grids with solid lines for current frame AOD_t and next frame AOD_{t+1} represent AOD image pairs with different resolutions, and the dashed lines indicate the resample procedure during image pyramid construction.

different humidity conditions, in accordance with the GOES-Chem AOD calculation algorithm (Jaeglé et al., 2011; Koepke et al., 1997; Martin et al., 2003). Validation of the model-simulated column AOD is conducted against AERONET AOD observations during the experimental period, as illustrated in Supplementary Material Fig. S1.

3.4. Aerosol transport quantification strategy

To quantify aerosol transport using the aerosol dynamic optical flow calculation based on temporally continuous AOD observations, an aerosol transport index (ATI) is defined in this study to quantitatively characterize the aerosol transport process, similar as the flux calculation approach using model simulations (Chakraborty et al., 2021; Chang et al., 2018). To provide a consistent description between the satellite-based optical flow results and the model-based results, the optical flow derived ATI and the model-derived ATI are unified spatially and temporally. As illustrated in Fig. 4, the optical-flow-derived ATI, which is an hourly summation of 10-min optical flow results, is calculated by firstly summing six 10-min calculation results in one hour, and then converting the length unit.

$$OpticalFlow\_ATI_{(x,y)} = \frac{1}{H} \bullet \sum_{t=1}^{6} Column\_AOD_{(x,y,t)} \bullet \overrightarrow{OF\_Vel_{(x,y,t)}} \bullet \lambda \quad (8)$$

where $AOD_{(x,y,t)}$ is the valid AOD value extracted from the AHI 10-min AOD dataset after recovery process located on (x,y) at time t; H is a constant indicating the height of entire AOD column; $\overrightarrow{OF\_Vel_{(x,y,t)}}$ is the pixel-based vector of the optical flow motion displacement for 10 min located on (x,y) estimated between the current AOD image (AOD_t) and subsequent AOD image (AOD_{t+1}); λ is a scaling constant that converts the unit of optical flow length from pixels to kilometers; and $t \in [1,6]$ represents the six 10-min observing moments in one designated hour. The model-based ATI is obtained by summing the simulated results of each vertical layer for the entire vertical column and then normalizing it to unit height, which can be expressed as:

$$Model\_ATI_{(x,y)} = \frac{1}{H} \bullet \sum_{h=1}^{14} AOD_{(x,y,h)} \bullet \overrightarrow{Wind\_Vel_{(x,y,h)}} \quad (9)$$

where $AOD_{(x,y,h)}$ is the hourly averaged WRF-CMAQ model simulated AOD vertical segment located on (x,y) in the vertical layer h for the corresponding hour, $\overrightarrow{Wind\_Vel_{(x,y,h)}}$ is the vector of WRF-simulated horizontal wind velocity located on (x,y) in the vertical layer h, and $h \in [1,14]$ represents the 14 sigma vertical layers defined in the WRF-CMAQ model configuration.

The ATI can be physically interpreted as aerosol mass extinction coefficient (α_{ext}, unit: km^2/g) multiplying the aerosol mass transport flux (F, unit: $g \bullet km^{-2} \bullet hour^{-1}$) as Eq. (10).

$$ATI = \epsilon_{ext} \bullet Vel = \alpha_{ext} \bullet C \bullet Vel = \alpha_{ext} \bullet F \quad (10)$$

where ϵ_{ext} here represents the aerosol extinction coefficient; Vel is the aerosol horizontal motion velocity; C is the aerosol mass concentration. As the aerosol mass extinction coefficient depends on the composition and size distribution of atmospheric pollutants, the ATI is proportional to F for the same atmospheric pollution plume, in which the aerosol mass extinction coefficient is a constant. Therefore, the ATI proposed in this study could be considered as a proxy that proportionally represents the aerosol mass transport flux to a certain extent. The derivation processes with corresponding explanations and references are included in the Supplementary Material Text S4. It should be noted that the ATI defined in this study represents the vertically normalized aerosol transport flux, since the optical flow algorithm is based on column AOD dataset without information about aerosol vertical distribution. In practical applications, the index ATI should be used in conjunction with the column height H rather than being used individually. Accordingly, the total aerosol loading crossing the entire grid boundary, illustrated as the shaded surface perpendicular to the ground surface in Fig. 4, over a period of time T can be calculated by multiplying the ATI by the cross sectional area of grid boundary and time, as expressed in Eq. (11).

$$Transported\ Aerosol\ Loading = ATI \bullet (L \bullet H) \bullet T \quad (11)$$

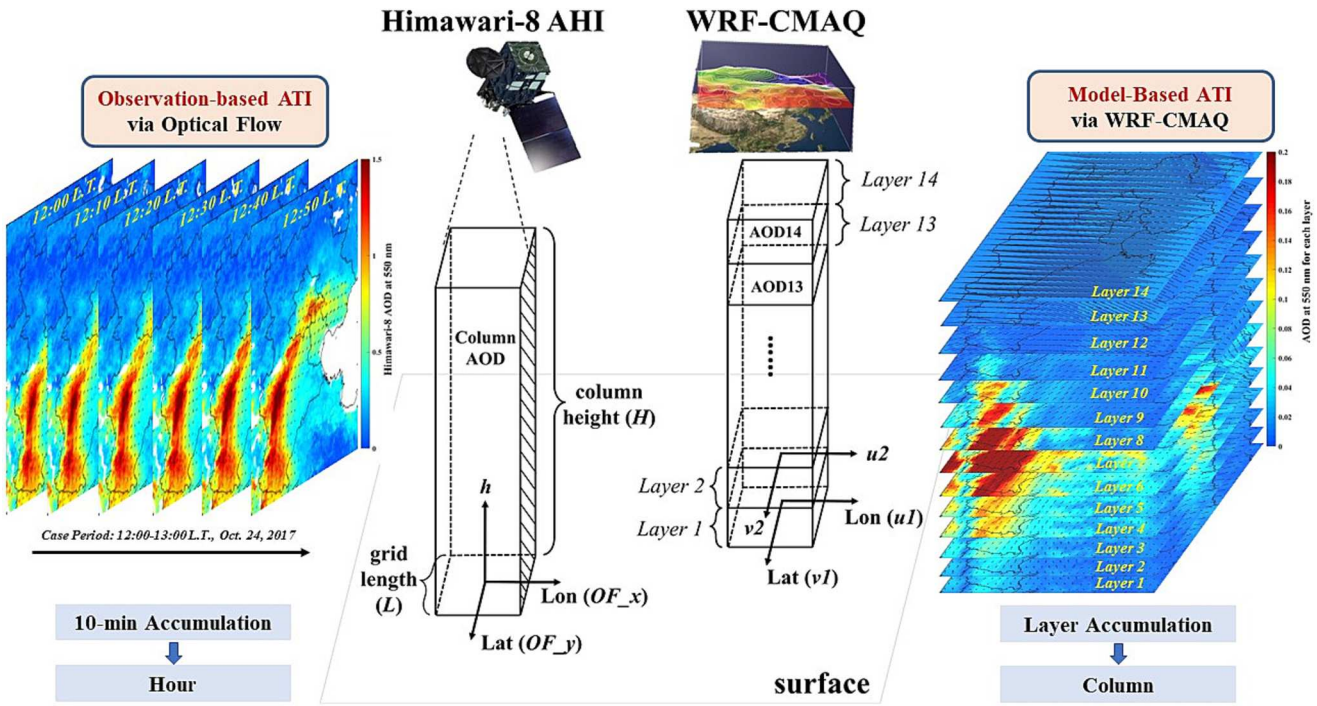

Fig. 4. Schematics of the observation-based quantification of aerosol transport, together with the comparison strategy against the results simulated by the WRF-CMAQ model.

where L is the grid length of geographic grid, and H is the column height. The unit for transported aerosol loading in terms of aerosol optical depth is $\left(km^2/g\right) \bullet g$, which proportionally represents the aerosol mass loading transporting between spatially adjacent geographic grids over a certain period of time, as the α_{ext} could be considered as a proportional constant between transported aerosol loading and transported aerosol mass loading for the same atmospheric pollution plume. Thus, the ATI can be used to characterize the interregional transport patterns of atmospheric pollutants based on long-term observations, which provides observation-based data support for policy and decision on regional atmospheric pollution joint control, as demonstrated by the case analyses in the section 4.3.

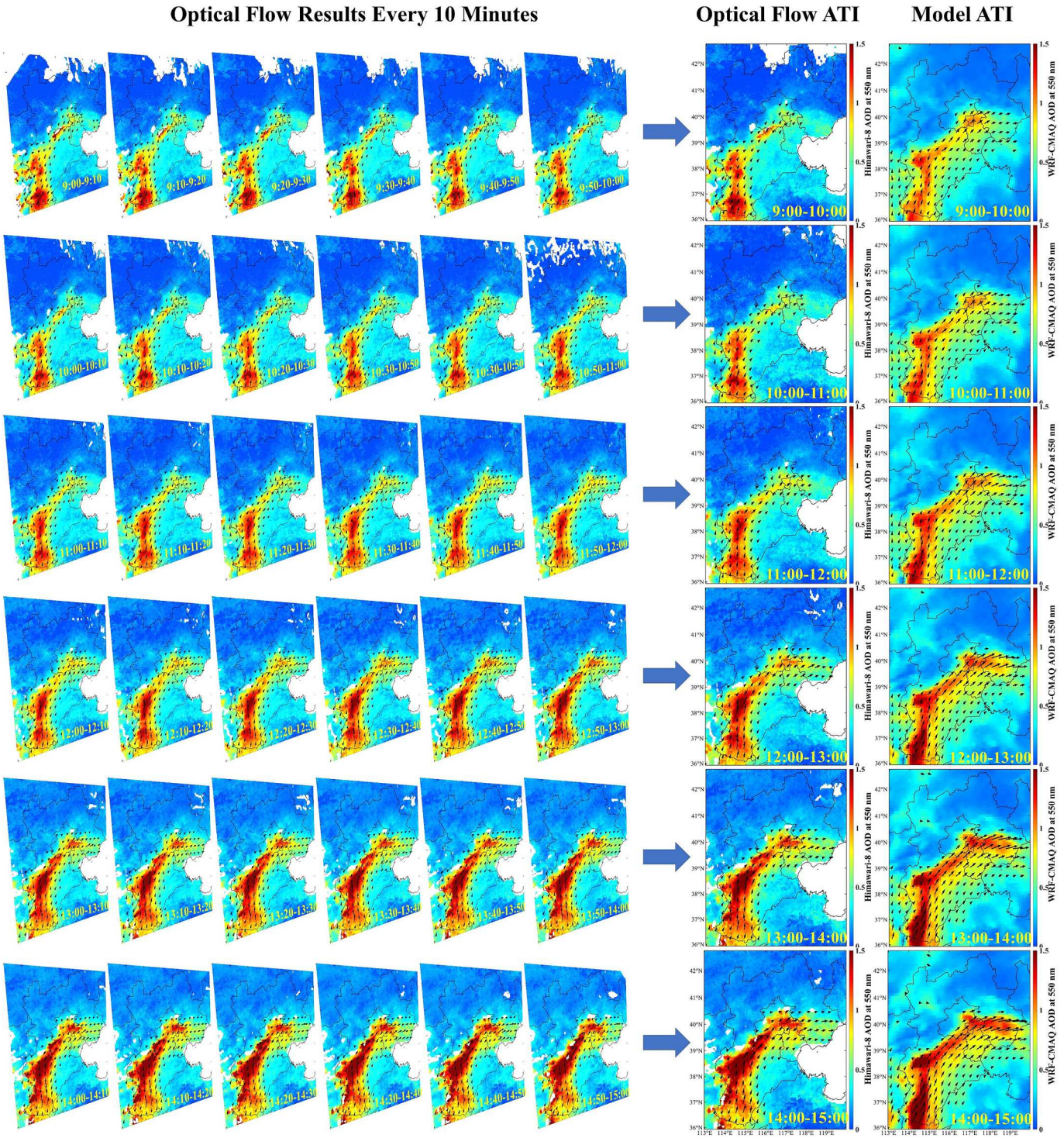

Fig. 5. The 10-min optical flow results and hourly integrated ATI (arrows), together with the corresponding AOD maps (color shading), illustrating the atmospheric pollution transport process toward the north and northeast on 24 October 2017, combined with the model-based ATI results.

4. Results and discussion

4.1. Satellite-based quantification of atmospheric pollution transport

The satellite-based 10-min optical flow transport results and hourly integrated ATI, together with the corresponding AOD maps, presented in Fig. 5, illustrate an atmospheric pollution transport processes during a haze event that occurred on 24 October 2017 over the BTH region. Similar to the conventional approach of representing the wind field in atmospheric physics and meteorology, the optical flow ATI estimated in this study is also indicated by arrows, where the transport direction and transport velocity calculated by the aerosol dynamic optical flow algorithm are represented by the arrow direction and arrow length, respectively. It is shown that both optical flow and model-based estimation results capture the atmospheric pollution transport process from southern Hebei Province toward the north and northeast in this case, which lead to the observed aggravation of air pollution in Beijing. Although physicochemical development and morphological variation of the polluted air mass occurred during the transport process, the aerosol dynamic optical flow method possesses the capability to distinguish the transport process from other dynamic processes of haze development. Moreover, it is crucial that the observing frequency exceeds the regular time interval over which an aerosol field might change obviously from the perspective of motion analysis, indicating that the proposed method can capture and describe the continuous spatiotemporal variations of atmospheric pollution transport, as clearly evident in Supplementary Material Animation S1. Additionally, the optical flow estimation results could further characterize the atmospheric pollution transport patterns, such as the loading of aerosol flowing into Beijing from southwestern Beijing boundary after noon, contributing significantly to the haze event in Beijing later in that day, is much larger than the inflow aerosol loading in the morning. However, the model-based results just describe the atmospheric pollution transport process in a relatively even way, namely quantifying the aerosol inflow transport process in an approximate rate, obtaining similar final haze result yet missing the fast-changing details of transport processes, which indicates that the aerosol dynamic optical flow algorithm based on high-frequency observations possesses unique advantages in capturing and characterizing the fast-changing processes of atmospheric pollution when comparing to the model-based method.

4.2. Comparison of the performance of the optical flow method and the model simulation

The satellite-based optical flow method could not only qualitatively capture the atmospheric pollution transport process, but also quantitatively describe the transport velocity for each pixel, thereby characterizing the transported aerosol loading via the ATI for each geographic grid. The robustness and reliability of the adopted optical flow assumption equation with similar constraint and regularization terms have been demonstrated in a series of practical scenes, including motion estimation for both rigid body and fluids (Cai et al., 2017b; Molnár et al., 2010; Ruhnau et al., 2005). Admittedly, the traditional optical flow verification approaches, typically including manual annotation for rigid motion and fluorescent tracking for nonrigid motion (Baker et al., 2011; Liu et al., 2008; Mayer et al., 2018), are not applicable for validation of the aerosol optical flow transport results. Since atmospheric aerosol is one type of fluids, we can neither precisely mark the displacement (probably with subpixel coordinates) for each AOD pixel between two temporally adjacent AOD frames, nor fluorescently label aerosols at such a large spatial scale and then track them through satellite images. Thus, in this study, selected results from WRF-CMAQ model simulation with ensured accuracy compared to the AOD observations are employed to calculate the ATI and transported aerosol loading as a reliable benchmark to cross-check the corresponding results derived from the optical flow algorithm. Validation against the AERONET observations shown in Supplementary Material Fig. S1 revealed that the accuracy of model-simulated AOD is not stable throughout the entire experimental period. The inferiority of the simulated results from the chemical transport models was primarily attributable to two aspects: the temporal shift during the model simulation and the uncertainty of emission sources that leads to over/underestimation of aerosol loading. Accordingly, comparison of the hourly ATI estimated by optical flow method and that by model simulation is conducted for the longitudinal (u) and latitudinal (v) directions in this study, only when the WRF-CMAQ model obtained accurate AOD within the expected error envelope (Levy et al., 2013; Sayer et al., 2014) and with almost no temporal shift. As illustrated in Fig. 6a and b, the comparison indicates that the optical-flow-derived ATI is well correlated with the model-derived ATI in both longitudinal and latitudinal directions, with a regression coefficient R^2 over 0.7. It demonstrates the effectiveness of the ATI in quantifying the aerosol transport rate, when utilizing pixel motion estimation in the proposed optical flow framework to represent the physical characteristics of column aerosol flow.

To some extent, a temporal shift usually exists in the model simulation, as exemplified in Supplementary Material Animation S2. Thus, the daily total transported aerosol loading from the satellite-based optical flow method is compared with that from the model simulation, which requires only that the daily averaged AOD from the WRF-CMAQ simulation is within the expected error envelope, while allowing a certain temporal shift in the model simulation. The daily total transported aerosol loading is estimated using all the valid values of ATI via Eq. (11) for each pixel in daytime in both the longitudinal (u) and the latitudinal (v) directions. Overall, approximately one hundred thousand matchups that meet the comparison criteria are included in the comparison. As shown in Fig. 7a and b, the daily total transported aerosol loading estimated via optical flow are slightly lower than those from the WRF-CMAQ simulation; however, they are well correlated with R^2 values of 0.647 and 0.734 in the longitudinal and latitudinal directions, respectively. This result indicates that the satellite-based optical flow method can achieve transported aerosol loading results comparable with those of widely accepted model-based methods, with a correlation coefficient R over 0.8.

4.3. Assessment of interregional transport of atmospheric pollution for Beijing

In the application case analyses illustrated in Fig. 8 and Fig. 9, atmospheric pollution inflow and outflow are estimated using the ATI for each boundary of Beijing, namely the Eastern boundary (marked in red), the Southern boundary (marked in grey), and the Northern and Western Boundary (marked in blue), which are defined based on both topographical factors and the bordering administrative cities. The calculation of inflow and outflow via ATI involves discretizing the vertical surface of the geographic grid according to the administrative boundary, as shown in Fig. 8b, where the vector linking inside and outside regions of a city is used to define the inflow and outflow of atmospheric pollution transport. Fig. 8c and d illustrate the daily averaged transported aerosol loadings for each boundary of Beijing, including aerosol inflow and outflow, on Oct. 24, 2017, which are calculated using ATI derived from both the optical flow and the WRF-CMAQ model. On this particular day, it is shown that the aerosol inflow overwhelms the aerosol outflow. The Southern Boundary of Beijing acts as the primary entrance for atmospheric pollution inflow, with the majority of pollutants stagnating locally. Only a minority of aerosols flows out through the Eastern Boundary of Beijing. The comparison results indicate there exist slight value differences of aerosol inflow/outflow loadings between optical flow method and model simulation in this case. These discrepancies may arise from the incapability of optical flow algorithm over slight pollution areas (such as part of the Northern and Western Boundary over the mountain regions) and potential biases in model simulated AOD (e.g., slightly overestimation in part of the Eastern Boundary in model

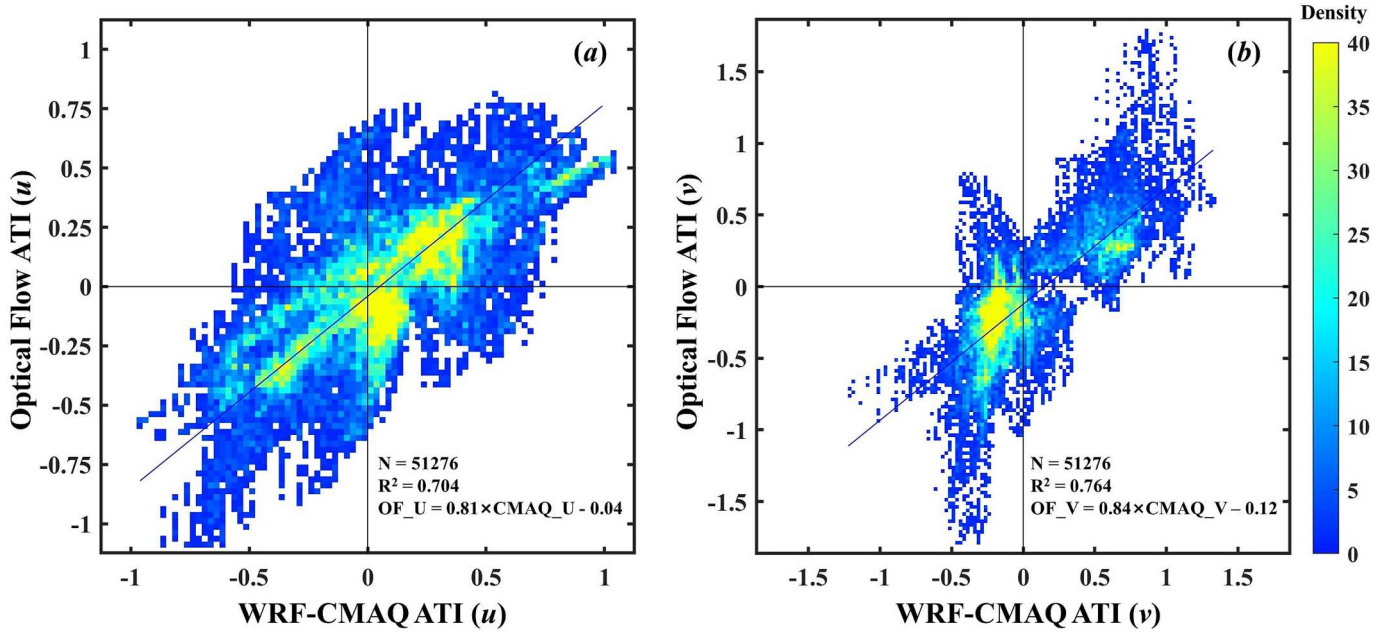

Fig. 6. Comparison of optical-flow-derived ATI and WRF-CMAQ-derived ATI in the (a) longitudinal direction and (b) latitudinal direction only when the WRF-CMAQ model performs well with neither over/underestimation of aerosol loading nor obvious temporal shift.

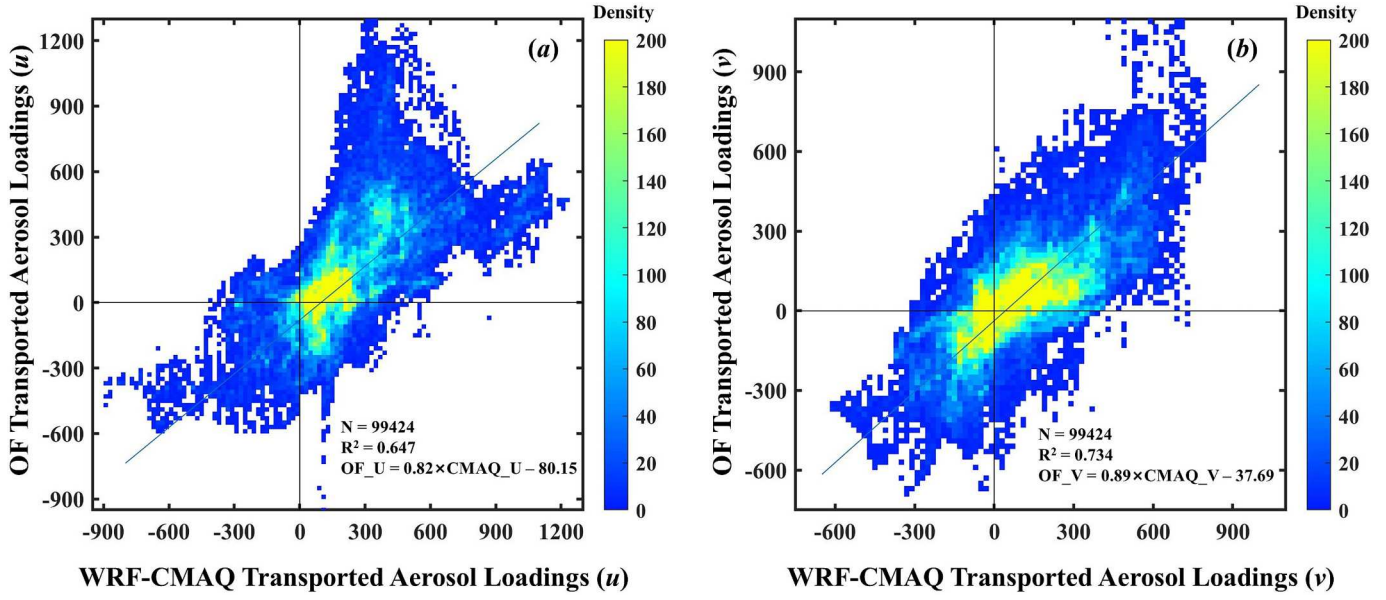

Fig. 7. Comparison of optical-flow-derived estimations and WRF-CMAQ simulations of the daily total transported aerosol loadings in the (a) longitudinal direction and (b) latitudinal direction when the WRF-CMAQ model obtains relatively accurate daily averaged AOD.

simulation). Despite these differences, the satellite-based optical flow method yields comparable aerosol transport patterns to those obtained by the model-based method on the day with ensured model simulated accuracy.

As illustrated in Fig. 9, the interregional transport characteristics of atmospheric pollution has been assessed for Beijing using the transported aerosol loading calculated via the optical flow framework based on 5-year satellite observations. The Fig. 9a and b illustrate the seasonal inflow and outflow transport contribution of each boundary of Beijing. As shown in Fig. 9a, the Southern boundary (Baoding and Langfang) is a main entrance for air pollution inflow, which takes up approximately 50 % of the inflow atmospheric pollution for Beijing, where the maximum contribution ratio appearing in summer while the minimum contribution ratio appearing in autumn. As shown in Fig. 9b, the Northern and Western boundary (Zhangjiakou and Chengde) is a main entrance for air pollution outflow, especially in winter which possesses nearly half contribution for atmospheric outflow, followed by Southern boundary and then Eastern boundary. Moreover, the multi-year trend of the annually averaged transported aerosol net loadings for Beijing from 2016 to 2020, as illustrated in Fig. 9c, can be obtain by subtracting the aerosol outflow loading from the aerosol inflow loading, where the positive/negative value indicates inflow/outflow dominance. The five-year net transport loadings show that atmospheric pollution inflows of Beijing typically exceed the outflows, indicating that Beijing acts as a "sink" of atmospheric pollution. The probable reason is that Beijing is half surrounded by western and northern mountains, where the

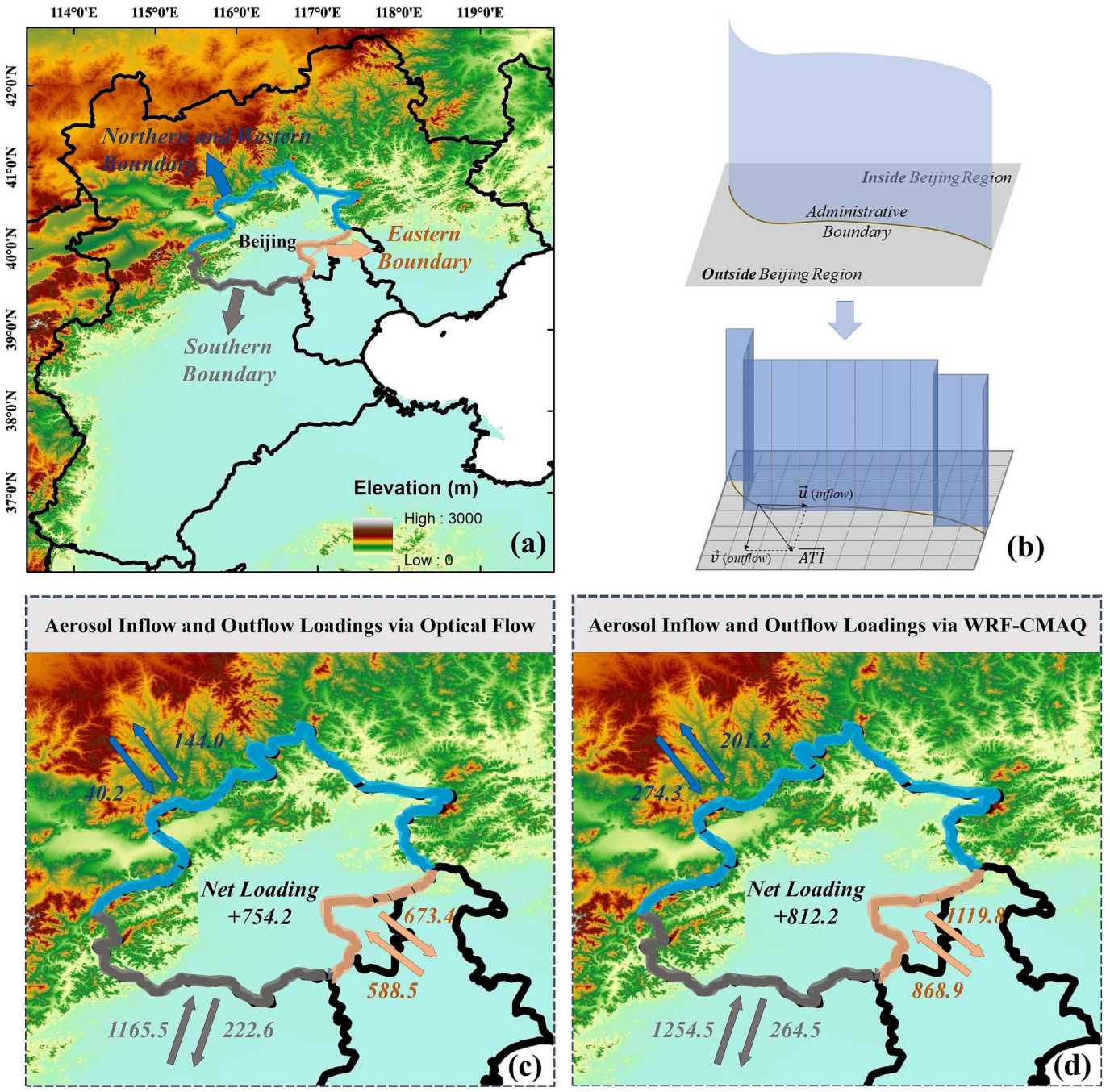

Fig. 8. The definition of three typical transport boundary of Beijing (a) with a discretization diagram of the vertical surface for inflow/outflow calculation (b). The daily averaged transported aerosol loadings for each boundary of Beijing as aerosol inflow and aerosol outflow on Oct. 24, 2017, which are calculated using ATI derived from optical flow (c) and WRF-CMAQ model (d).

atmospheric pollution is possibly blocked by the bulging part of the plain. The trapped atmospheric pollution could be removed by vertical convection dilution effect resulted from relatively strong northwestern wind, or by the scavenging effect from precipitation. Furthermore, a generally downward trend could be found from the year-by-year trend of annually averaged transported aerosol net loadings from 2016 to 2020, which demonstrates the effectiveness of emission reduction policy in BTH regions. Comparing to model simulation that requires high computational performance to calculate and consumes considerable human resources to update the emission source inventory, the satellite-based optical flow method, benefit from low-cost calculation and large-scale satellite observation, could offer a more economical and efficient way for assessing the interregional transport of atmospheric pollution and regional joint control policy.

5. Conclusion and future work

Interregional transport plays an important role in local atmospheric pollution with varying contribution extent under different meteorological and emission conditions. Current studies on quantitatively analyzing interregional atmospheric pollution transport have mainly relied on meteorological and chemical models. However, these models are typically affected by uncertainties due to the assumptions and simplifications inherent in the numerical simulations and source emission estimations. This study develops a comprehensive optical flow framework to offer a new perspective to provide observation-based

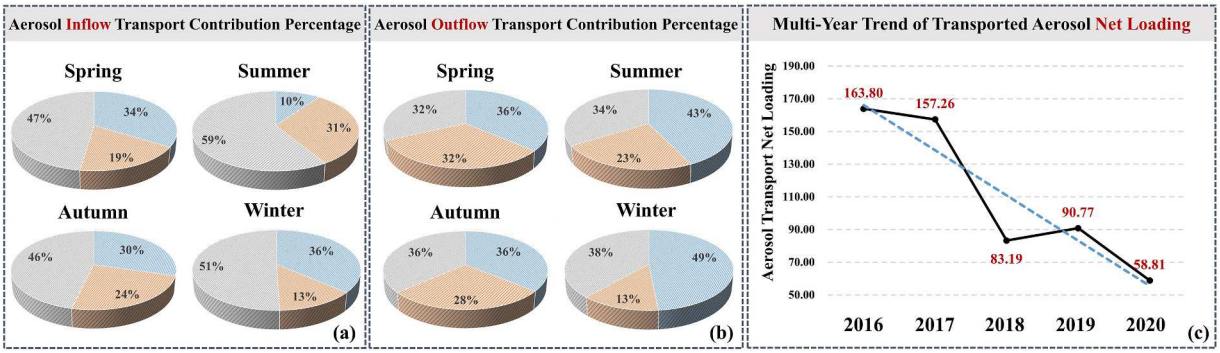

Fig. 9. The aerosol inflow and outflow transport contribution percentage for each boundary of Beijing are illustrated in the subgraphs (a) and (b), while the multi-year trend of annually averaged transported aerosol net loadings for Beijing from 2016 to 2020 is demonstrated in the subplot (c).

quantification of aerosol transport and characterize interregional transport patterns of atmospheric pollution using synergistic observations from geostationary and sun-synchronous satellite sensors. Experimental results demonstrate that the proposed aerosol dynamic optical flow method possesses the capability to distinguish the transport process from other dynamic processes of aerosol development, and could capture and describe the continuous spatiotemporal variations as well as the fast-changing details of aerosol transport. Moreover, comparison of the atmospheric pollution transport results estimated via optical flow and via model simulations shows reasonable agreements with a correlation coefficient R over 0.8 in both longitudinal and latitudinal directions, highlighting the effectiveness of the developed optical flow framework in quantitative characterization of the atmospheric pollution transport process via the ATI and transported aerosol loadings. Furthermore, a case analysis of long-term assessments of interregional transport of atmospheric pollution for Beijing indicates that Beijing acts as a "sink" of atmospheric pollution, but a downward trend could be found from the year-by-year trend of annually averaged transported aerosol net loadings from 2016 to 2020, due to the emission reduction policy over the BTH regions. Compared with model-based methods, the satellite-based optical flow framework is directly grounded in observations and does not rely on emission inventories that take years to update. Benefiting from near-real-time and large-scale satellite observations, it not only helps improve understanding the patterns of atmospheric pollution interregional transport, but also provides a more efficient and economical way to assess the effectiveness of regional joint control policy.

In this study, the BTH region is selected as representative of areas having air quality concerns with typical topographic characteristics. Obviously, the proposed satellite-based optical flow framework is also applicable to extend to other regions with atmospheric pollution issues. Admittedly, certain limitations exist in current aerosol dynamic optical flow algorithm. For example, there is still a certain area of data blanks in AOD datasets that restrict the availability of the proposed algorithm. Besides, the aerosol transport discussed in this study represents the overall aerosol movement across the entire atmospheric column, since current calculations rely on column AOD fusion datasets due to the limitations in terms of spatial coverage and observing frequency associated with the CALIOP aerosol profile observations. Future work could incorporate additional aerosol–cloud satellite and ground-based active sensors into the framework to recover additional aerosol information in the case of cloud obscuration, and to provide more vertical information for possible analyses on aerosol vertical distribution characteristics during transport. Additionally, combining the proposed satellite-based optical flow method with a traditional model-based method might help improve understanding the patterns of atmospheric pollution interregional transport and its contribution to local haze event.

Supplementary data to this article can be found online at https://doi.org/10.1016/j.rse.2024.114457.

CRediT authorship contribution statement

Tianhao Zhang: Writing – review & editing, Writing – original draft, Visualization, Validation, Methodology, Conceptualization. **Yu Gu:** Writing – review & editing, Validation, Conceptualization. **Bin Zhao:** Writing – review & editing, Validation, Methodology, Conceptualization. **Lunche Wang:** Writing – review & editing, Validation. **Zhongmin Zhu:** Writing – review & editing, Validation. **Yun Lin:** Writing – review & editing, Validation. **Xing Chang:** Validation, Software. **Xinghui Xia:** Writing – review & editing, Visualization, Validation, Methodology. **Zhe Jiang:** Writing – review & editing, Validation. **Hongrong Shi:** Writing – review & editing, Validation, Conceptualization. **Wei Gong:** Writing – review & editing, Validation, Conceptualization.

Declaration of competing interest

The authors declare that they have no known competing financial interests or personal relationships that could have appeared to influence the work reported in this paper.

Data availability

Data will be made available on request.

Acknowledgment

This work was supported by the US NSF grants (AGS-2345272), the National Natural Science Foundation of China (No. 42071353), and the China Postdoctoral Science Foundation (No. 2020 M682486). The authors would like to express their gratitude to the JAXA for providing Himawari-8 AHI data, NASA for providing Terra/Aqua MODIS and CALIPSO CALIOP datasets, and the Principle Investigators for establishing and maintaining the AERONET network. The MODIS data used in this study were downloaded from the NASA LAADS DAAC data archive (available at https://ladsweb.modaps.eosdis.nasa.gov/search/, last accessed on 7 March 2024). The Himawari-8 AHI datasets were obtained from https://www.eorc.jaxa.jp/ptree/ (last accessed on 7 March 2024). The CALIPSO datasets used in this study are available at https://www-calipso.larc.nasa.gov/products/ (last accessed on 7 March 2024).

References

Albrecht, B.A., 1989. Aerosols, cloud microphysics, and fractional cloudiness. Science 245, 1227–1230.
Aubin, J.-P., 2011. Applied Functional Analysis. John Wiley & Sons.
Baker, S., Scharstein, D., Lewis, J.P., Roth, S., Black, M.J., Szeliski, R., 2011. A database and evaluation methodology for optical flow. Int. J. Comput. Vis. 92, 1–31.
Barron, J.L., Fleet, D.J., Beauchemin, S.S., 1994. Performance of optical-flow techniques. Int. J. Comput. Vis. 12, 43–77.
Beauchemin, S.S., Barron, J.L., 1995. The computation of optical flow. ACM Comput. Surv. 27, 433–467.

Berge, E., Jakobsen, H.A., 1998. A regional scale multi-layer model for the calculation of long-term transport and deposition of air pollution in Europe. Tellus Series B-Chem. Phys. Meteorol. 50, 205–223.
Bessho, K., Date, K., Hayashi, M., Ikeda, A., Imai, T., Inoue, H., Kumagai, Y., Miyakawa, T., Murata, H., Ohno, T., Okuyama, A., Oyama, R., Sasaki, Y., Shimazu, Y., Shimoji, K., Sumida, Y., Suzuki, M., Taniguchi, H., Tsuchiyama, H., Uesawa, D., Yokota, H., Yoshida, R., 2016. An introduction to Himawari-8/9-Japan's new-generation geostationary meteorological satellites. J. Meteorol. Soc. Jpn. 94, 151–183.
Brox, T., Bruhn, A., Papenberg, N., Weickert, J., 2004. High accuracy optical flow estimation based on a theory for warping. In: Computer Vision - Eccv 2004, Pt 4, 2034, pp. 25–36.
Cai, S.Y., Wang, Y.J., Zhao, B., Wang, S.X., Chang, X., Hao, J.M., 2017a. The impact of the "air pollution prevention and control action plan" on PM2.5 concentrations in Jing-Jin-Ji region during 2012-2020. Sci. Total Environ. 580, 197–209.
Cai, S.Z., Huang, Y.B., Ye, B., Xu, C., 2017b. Dynamic illumination optical flow computing for sensing multiple Mobile robots from a drone. In: Ieee Transactions on Systems Man Cybernetics-Systems, 48, pp. 1370–1382.
Campbell, J.R., Tackett, J.L., Reid, J.S., Zhang, J., Curtis, C.A., Hyer, E.J., Sessions, W.R., Westphal, D.L., Prospero, J.M., Welton, E.J., Omar, A.H., Vaughan, M.A., Winker, D. M., 2012. Evaluating nighttime CALIOP 0.532 μm aerosol optical depth and extinction coefficient retrievals. Atmos. Meas. Tech. 5, 2143–2160.
Chakraborty, S., Guan, B., Waliser, D.E., da Silva, A.M., Uluatam, S., Hess, P., 2021. Extending the Atmospheric River concept to aerosols: climate and air quality impacts. Geophys. Res. Lett. 48.
Chang, X., Wang, S.X., Zhao, B., Cai, S.Y., Hao, J.M., 2018. Assessment of inter-city transport of particulate matter in the Beijing-Tianjin-Hebei region. Atmos. Chem. Phys. 18, 4843–4858.
Chang, X., Wang, S.X., Zhao, B., Xing, J., Liu, X.X., Wei, L., Song, Y., Wu, W.J., Cai, S.Y., Zheng, H.T., Ding, D., Zheng, M., 2019. Contributions of inter-city and regional transport to PM2.5 concentrations in the Beijing-Tianjin-Hebei region and its implications on regional joint air pollution control. Sci. Total Environ. 660, 1191–1200.
Christakos, G., 2002. On the assimilation of uncertain physical knowledge bases: Bayesian and non-Bayesian techniques. Adv. Water Resour. 25, 1257–1274.
Christakos, G., Li, X.Y., 1998. Bayesian maximum entropy analysis and mapping: a farewell to kriging estimators? Math. Geol. 30, 435–462.
Christopher, S.A., Jones, T.A., 2010. Satellite and surface-based remote sensing of Saharan dust aerosols. Remote Sens. Environ. 114, 1002–1007.
Cohen, A.J., Brauer, M., Burnett, R., Anderson, H.R., Frostad, J., Estep, K., Balakrishnan, K., Brunekreef, B., Dandona, L., Dandona, R., Feigin, V., Freedman, G., Hubbell, B., Jobling, A., Kan, H., Knibbs, L., Liu, Y., Martin, R., Morawska, L., Pope, C., Shin, H., Straif, K., Shaddick, G., Thomas, M., van Dingenen, R., van Donkelaar, A., Vos, T., Murray, C.J.L., Forouzanfar, M.H., 2017. Estimates and 25-year trends of the global burden of disease attributable to ambient air pollution: an analysis of data from the global burden of diseases study 2015. Lancet 389, 1907–1918.
Ding, D., Xing, J., Wang, S.X., Liu, K.Y., Hao, J.M., 2019. Estimated contributions of emissions controls, meteorological factors, population growth, and changes in baseline mortality to reductions in ambient PM2.5 and PM2.5-related mortality in China, 2013-2017. Environ. Health Perspect. 127.
Ding, D., Xing, J., Wang, S.X., Dong, Z.X., Zhang, F.F., Liu, S.C., Hao, J.M., 2022. Optimization of a NOx and VOC cooperative control strategy based on clean air benefits. Environ. Sci. Technol. 56, 739–749.
Draxler, R.R., Hess, G.D., 1998. An overview of the HYSPLIT_4 modelling system for trajectories, dispersion and deposition. Aust. Meteorol. Mag. 47, 295–308.
Fleet, D., Weiss, Y., 2006. Optical flow estimation. In: Handbook of Mathematical Models in Computer Vision. Springer, pp. 237–257.
Gibson, J.J., 1950. The Perception of the Visual World.
Gupta, P., Levy, R.C., Mattoo, S., Remer, L.A., Holz, R.E., Heidinger, A.K., 2019. Applying the dark target aerosol algorithm with advanced Himawari imager observations during the KORUS-AQ field campaign. Atmos. Meas. Tech. 12, 6557–6577.
Han, L.H., Cheng, S.Y., Zhuang, G.S., Ning, H.B., Wang, H.Y., Wei, W., Zhao, X.J., 2015. The changes and long-range transport of PM2.5 in Beijing in the past decade. Atmos. Environ. 110, 186–195.
Horn, B.K., Schunck, B.G., 1981. Determining optical flow. Artif. Intell. 17, 185–203.
Hsu, N.C., Jeong, M.J., Bettenhausen, C., Sayer, A.M., Hansell, R., Seftor, C.S., Huang, J., Tsay, S.C., 2013. Enhanced deep blue aerosol retrieval algorithm: the second generation. J. Geophys. Res.-Atmos. 118, 9296–9315.
Huang, Y., Zhu, B., Zhou, X., Chen, D., Zhu, Z., Zhang, T., Gong, W., Ji, Y., Xia, X., Wang, L., 2019. Evaluation and comparison of MODIS collection 6.1 and collection 6 dark target aerosol optical depth over mainland China under various conditions including spatiotemporal distribution, haze effects, and underlying surface. Earth and Space Sci. 6, 2575–2592.
Huang, X., Ding, A.J., Wang, Z.L., Ding, K., Gao, J., Chai, F.H., Fu, C.B., 2020. Amplified transboundary transport of haze by aerosol-boundary layer interaction in China. Nat. Geosci. 13, 428–434.
Ishida, H., Nakajima, T.Y., 2009. Development of an unbiased cloud detection algorithm for a spaceborne multispectral imager. J. Geophys. Res.-Atmos. 114.
Jaeglé, L., Quinn, P.K., Bates, T.S., Alexander, B., Lin, J.T., 2011. Global distribution of sea salt aerosols: new constraints from in situ and remote sensing observations. Atmos. Chem. Phys. 11, 3137–3157.
Jenner, S.L., Abiodun, B.J., 2013. The transport of atmospheric sulfur over Cape Town. Atmos. Environ. 79, 248–260.
Kacenelenbogen, M., Vaughan, M.A., Redemann, J., Hoff, R.M., Rogers, R.R., Ferrare, R. A., Russell, P.B., Hostetler, C.A., Hair, J.W., Holben, B.N., 2011. An accuracy assessment of the CALIOP/CALIPSO version 2/version 3 daytime aerosol extinction product based on a detailed multi-sensor, multi-platform case study. Atmos. Chem. Phys. 11, 3981–4000.
Kan, H.D., Chen, R.J., Tong, S.L., 2012. Ambient air pollution, climate change, and population health in China. Environ. Int. 42, 10–19.
Kikuchi, M., Murakami, H., Suzuki, K., Nagao, T.M., Higurashi, A., 2018. Improved hourly estimates of aerosol optical thickness using spatiotemporal variability derived from Himawari-8 geostationary satellite. IEEE Trans. Geosci. Remote Sens. 56, 3442–3455.
Knippertz, P., Evans, M.J., Field, P.R., Fink, A.H., Liousse, C., Marsham, J.H., 2015. The possible role of local air pollution in climate change in West Africa. Nat. Clim. Chang. 5, 815–822.
Koepke, P., Hess, M., Schult, I., Shettle, E.P., 1997. Global Aerosol Data Set.
Levy, R.C., Remer, L.A., Mattoo, S., Vermote, E.F., Kaufman, Y.J., 2007. Second-generation operational algorithm: retrieval of aerosol properties over land from inversion of moderate resolution imaging Spectroradiometer spectral reflectance. J. Geophys. Res.-Atmos. 112.
Levy, R.C., Mattoo, S., Munchak, L.A., Remer, L.A., Sayer, A.M., Patadia, F., Hsu, N.C., 2013. The collection 6 MODIS aerosol products over land and ocean. Atmos. Meas. Tech. 6, 2989–3034.
Li, P.F., Yan, R.C., Yu, S.C., Wang, S., Liu, W.P., Bao, H.M., 2015. Reinstate regional transport of PM2.5 as a major cause of severe haze in Beijing. Proc. Natl. Acad. Sci. USA 112, E2739–E2740.
Liu, C., Freeman, W.T., Adelson, E.H., Weiss, Y., 2008. Human-assisted motion annotation. In: 2008 IEEE Conference on Computer Vision and Pattern Recognition, 1-12, pp. 3911–3918.
Lucas, B.D., Kanade, T., 1981. An iterative image registration technique with an application to stereo vision. In: IJCAI'81: 7th International Joint Conference on Artificial Intelligence, pp. 674–679.
Martin, R.V., Jacob, D.J., Yantosca, R.M., Chin, M., Ginoux, P., 2003. Global and regional decreases in tropospheric oxidants from photochemical effects of aerosols. J. Geophys. Res.-Atmos. 108.
Masson-Delmotte, V., Zhai, P., Pirani, A., Connors, S.L., Péan, C., Berger, S., Caud, N., Chen, Y., Goldfarb, L., Gomis, M., 2021. Climate Change 2021: The Physical Science Basis. Contribution of Working Group I to the Sixth Assessment Report of the Intergovernmental Panel on Climate Change, 2.
Mayer, N., Ilg, E., Fischer, P., Hazirbas, C., Cremers, D., Dosovitskiy, A., Brox, T., 2018. What makes good synthetic training data for learning disparity and optical flow estimation? Int. J. Comput. Vis. 126, 942–960.
Mhawish, A., Banerjee, T., Broday, D.M., Misra, A., Tripathi, S.N., 2017. Evaluation of MODIS collection 6 aerosol retrieval algorithms over indo-Gangetic plain: implications of aerosols types and mass loading. Remote Sens. Environ. 201, 297–313.
Molnár, J., Chetverikov, D., Fazekas, S., 2010. Illumination-robust variational optical flow using cross-correlation. Comput. Vis. Image Underst. 114, 1104–1114.
Pope, C.A., Burnett, R.T., Thun, M.J., Calle, E.E., Krewski, D., Ito, K., Thurston, G.D., 2002. Lung cancer, cardiopulmonary mortality, and long-term exposure to fine particulate air pollution. JAMA-J. American Med. Assoc. 287, 1132–1141.
Prather, K., 2009. Determination of the Spatial and Temporal Variability of Size-Resolved PM2. 5 Composition and Mixing State in Multiple Regions in California. California Air Resources Board.
Ramanathan, V., Crutzen, P.J., Kiehl, J.T., Rosenfeld, D., 2001. Atmosphere - aerosols, climate, and the hydrological cycle. Science 294, 2119–2124.
Ruhnau, P., Kohlberger, T., Schnörr, C., Nobach, H., 2005. Variational optical flow estimation for particle image velocimetry. Exp. Fluids 38, 21–32.
Sayer, A.M., Munchak, L.A., Hsu, N.C., Levy, R.C., Bettenhausen, C., Jeong, M.J., 2014. MODIS collection 6 aerosol products: comparison between Aqua's e-deep blue, dark target, and "merged" data sets, and usage recommendations. J. Geophys. Res.-Atmos. 119, 13965–13989.
Schnorr, C., 1991. Determining optical-flow for irregular domains by minimizing quadratic Functionals of a certain class. Int. J. Comput. Vis. 6, 25–38.
Spadavecchia, L., Williams, M., 2009. Can spatio-temporal geostatistical methods improve high resolution regionalisation of meteorological variables? Agric. For. Meteorol. 149, 1105–1117.
Stein, A.F., Draxler, R.R., Rolph, G.D., Stunder, B.J.B., Cohen, M.D., Ngan, F., 2015. Noaa's Hysplit atmospheric transport and dispersion modeling system. Bull. Am. Meteorol. Soc. 96, 2059–2077.
Tang, Q.X., Bo, Y.C., Zhu, Y.X., 2016. Spatiotemporal fusion of multiple-satellite aerosol optical depth (AOD) products using Bayesian maximum entropy method. J. Geophys. Res.-Atmos. 121, 4034–4048.
Vaughan, M.A., Powell, K.A., Kuehn, R.E., Young, S.A., Winker, D.M., Hostetler, C.A., Hunt, W.H., Liu, Z.Y., McGill, M.J., Getzewich, B.J., 2009. Fully automated detection of cloud and aerosol layers in the CALIPSO Lidar measurements. J. Atmos. Ocean. Technol. 26, 2034–2050.
Wang, K., Zhang, Y., Jang, C., Phillips, S., Wang, B.Y., 2009. Modeling intercontinental air pollution transport over the trans-Pacific region in 2001 using the community multiscale air quality modeling system. J. Geophys. Res.-Atmos. 114.
Xia, X.H., Zhao, B., Zhang, T.H., Wang, L.Y., Gu, Y., Liou, K.N., Mao, F.Y., Liu, B.M., Bo, Y.C., Huang, Y.S., Dong, J.D., Gong, W., Zhu, Z.M., 2021. Satellite-derived aerosol optical depth fusion combining active and passive remote sensing based on Bayesian maximum entropy. IEEE Trans. Geosci. Remote Sens. 60.
Xia, X.H., Zhang, T.H., Wang, L.C., Gong, W., Zhu, Z.M., Wang, W., Gu, Y., Lin, Y., Zhou, X.Y., Dong, J.D., Fan, S.M., Xu, W.F., 2023. Spatial-temporal fusion of 10-min aerosol optical depth products with the GEO-LEO satellite joint observations. Remote Sens. 15.

Yang, Y.J., Wilkinson, J.G., Russell, A.G., 1997. Fast, direct sensitivity analysis of multidimensional photochemical models. Environ. Sci. Technol. 31, 2859–2868.
Yoshida, M., Yumimoto, K., Nagao, T.M., Tanaka, T.Y., Kikuchi, M., Murakami, H., 2021. Satellite retrieval of aerosol combined with assimilated forecast. Atmos. Chem. Phys. 21, 1797–1813.
Yu, H.B., Remer, L.A., Chin, M., Bian, H.S., Tan, Q., Yuan, T.L., Zhang, Y., 2012. Aerosols from overseas rival domestic emissions over North America. Science 337, 566–569.
Zhang, H., DeNero, S.P., Joe, D.K., Lee, H.H., Chen, S.H., Michalakes, J., Kleeman, M.J., 2014. Development of a source oriented version of the WRF/Chem model and its application to the California regional PM10/PM2.5 air quality study. Atmos. Chem. Phys. 14, 485–503.
Zhang, Q., Jiang, X.J., Tong, D., Davis, S.J., Zhao, H.Y., Geng, G.N., Feng, T., Zheng, B., Lu, Z.F., Streets, D.G., Ni, R.J., Brauer, M., van Donkelaar, A., Martin, R.V., Huo, H., Liu, Z., Pan, D., Kan, H.D., Yan, Y.Y., Lin, J.T., He, K.B., Guan, D.B., 2017. Transboundary health impacts of transported global air pollution and international trade. Nature 543, 705–709.
Zhang, T.H., Zhu, Z.M., Gong, W., Zhu, Z.R., Sun, K., Wang, L.C., Huang, Y.S., Mao, F.Y., Shen, H.F., Li, Z.W., Xu, K., 2018. Estimation of ultrahigh resolution PM2.5 concentrations in urban areas using 160 m Gaofen-1 AOD retrievals. Remote Sens. Environ. 216, 91–104.
Zhang, T., Zhao, B., Gu, Y., Zhu, Z., Gong, W., Shi, H., Liou, K.-N., 2019. Assessments of haze transport in China via optical flow method based on satellite-retrieved AOD image sequences. In: AGU Fall Meeting Abstracts (pp. A12B-08).
Zhang, T., Zhao, B., Gu, Y., Zhu, Z., Gong, W., Liou, K.-N., 2020. Assessment of haze transport via multi-scale pyramid optical flow method based on satellite-retrieved AOD image sequences. In: AGU Fall Meeting Abstracts (pp. A026-003).
Zhang, T., Wang, L., Zhao, B., Gu, Y., Wong, M.S., She, L., Xia, X., Dong, J., Ji, Y., Gong, W., Zhu, Z., 2022. A geometry-discrete minimum reflectance aerosol retrieval algorithm (GeoMRA) for geostationary meteorological satellite over heterogeneous surfaces. IEEE Trans. Geosci. Remote Sens. 60.
Zhang, T.H., Shen, H.F., Xia, X.H., Wang, L.C., Mao, F.Y., Yuan, Q.Q., Gu, Y., Zhao, B., Zhu, Z.M., Lin, Y., Bo, Y.C., Gong, W., 2023. Himawari-8 high temporal resolution AOD products recovery: nested Bayesian maximum entropy fusion blending GEO with SSO satellite observations. IEEE Trans. Geosci. Remote Sens. 61.
Zhao, B., Wang, S.X., Xing, J., Fu, K., Fu, J.S., Jang, C., Zhu, Y., Dong, X.Y., Gao, Y., Wu, W.J., Wang, J.D., Hao, J.M., 2015. Assessing the nonlinear response of fine particles to precursor emissions: development and application of an extended response surface modeling technique v1.0. Geosci. Model Dev. 8, 115–128.
Zhao, B., Wang, Y., Gu, Y., Liou, K.N., Jiang, J.H., Fan, J.W., Liu, X.H., Huang, L., Yung, Y.L., 2019. Ice nucleation by aerosols from anthropogenic pollution. Nat. Geosci. 12, 602–607.